Pressure-driven metallization in hafnium diselenide

Adrián Andrada-Chacón,*,[†] Ángel Morales-García,[‡] Miguel A. Salvadó,[§] Pilar Pertierra,[§] Ruth Franco,[§] Gastón Garbarino,[‖] Mercedes Taravillo,[†] José A. Barreda-Argüeso,[#] Jesús González,[#] Valentín G. Baonza,[†] J. Manuel Recio,[§] Javier Sánchez-Benítez[†]

[†] MALTA-Consolider Team, Departamento de Química Física, Facultad de Ciencias Químicas, Universidad Complutense de Madrid, 28040-Madrid, Spain

[‡] Departament de Ciència de Materials i Química Física & Institut de Química Teòrica i Computacional (IQTCUB), Universitat de Barcelona, c/ Martí i Franquès, 1-11, 08028-Barcelona, Spain

[§] MALTA-Consolider Team, Departamento de Química Física y Analítica, Universidad de Oviedo, 33006-Oviedo, Spain

[‖] European Synchrotron Radiation Facility, BP 220, 6 Rue Jules Horowitz, 38043, Grenoble, Cedex 9, France

[#] MALTA-Consolider Team, CITIMAC, Universidad de Cantabria, Santander, Spain

Abstract

The quest for new transition metal dichalcogenides (TMDs) with outstanding electronic properties operating at ambient conditions draws us to investigate the 1T-$HfSe_2$ polytype under hydrostatic pressure. Diamond anvil cell (DAC) devices coupled to *in-situ* synchrotron X-ray, Raman and optical (VIS-NIR) absorption experiments along with density functional theory (DFT) based calculations prove that: (i) bulk 1T-$HfSe_2$ exhibits strong structural and vibrational anisotropies, being the interlayer direction especially sensitive to pressure changes, (ii) the indirect gap of 1T-$HfSe_2$ trend to vanish by a -0.1 eV/GPa pressure rate, slightly faster than MoS_2 or WS_2, (iii) the onset of the metallic behavior appears at P_{met} ~10 GPa, which is to date the lowest pressure among common TMDs, and finally (iv) the electronic transition is explained by the bulk modulus B_0-P_{met} correlation, along with the pressure coefficient of the band gap, in terms of the electronic overlap between chalcogenide *p*-type and metal *d*-type orbitals.

Overall, our findings identify 1T-$HfSe_2$ as a new efficient TMD material with potential multi-purpose technological applications.

INTRODUCTION

Layered based materials have attracted a tremendous research interest since the breakthrough of graphene.[1] These materials have been widely studied owing to the intrinsic electronic properties covering from semiconductivity to metallic behavior along with promising catalytic performance, photoluminescence, and high-water resistance.[2,3,4,5] Particularly, layered transition-metal dichalcogenides (TMDs) exhibit unique optical and electronic properties accompanied by a tunable band gap.[6] From the structural point of view, TMDs are defined as solids with the general stoichiometry MX_2 (M is a transition metal that belongs to the groups IV, V, VI, and VII; X=S, Se, Te) showing in-plane strong chemical bonding and out-of-plane weak van der Waals (vdW) interactions, as represented in Figure 1a. Based on the atomic arrangements, TMDs are classified in three stacking polytypes denoted as 1T, 2H and 3R that correspond to one, two and three layers per unit cell with trigonal, hexagonal and rhombohedral structure, respectively. Note however, that M_2X_3 and MX alternative stoichiometries have been recently found for TMDs.[7,8] There are roughly sixty TMDs known so far, but, since MoS_2, TiS_2 and WS_2 have attracted more attention, these three compounds are considered the workhorse among them.[9,10]

Not surprisingly, the structural and electronic properties of few layers and bulk TMDs can be easily tuned thanks to the abovementioned vdW interlayer forces.[11] Several strategies have been established to enhance their performance including (i) top-down synthesis protocols moving towards low-dimensional TMDs counterparts,[12] (ii) the use of chemical dopant agents,[13] (iii) the intercalation of species,[14] (iv) the application of

electrical field,[15] and (v) the application of high pressures.[16] The latter strategy brings the layers closer and, thus, making the interlayer interactions much stronger resulting in a concomitant modulation of the TMDs properties.

Recent experimental and theoretical investigations on the pressure-induced properties of bulk TMDs, such as MoS_2, WS_2, $MoSe_2$, WSe_2 and $MoTe_2$ have reported interesting semiconducting-to-metal electronic state transitions achieved at ~15–40 GPa under hydrostatic conditions, depending on the TMD composition.[17,18,19,20,21,22,23] The implementation of these results in flexible nanoelectronics devices involves practical difficulties mainly due to the high-pressure regimes required to induce the metallization.[24] To overcome this drawback, low-dimensional counterparts of TMDs coupled with uni- and bi-axial stress conditions have been proposed as a suitable alternative to modulate the band gap at lower pressures. Combined experimental and theoretical studies have successfully shown that the metallization of monolayer MoS_2 takes place only at 3 GPa under uniaxial out-of-plane compression conditions.[25,26]

All these extensive efforts have contributed significantly to the knowledge of bulk, few layer and monolayer TMDs under extreme conditions. Most of the studies have been focused only on the 2H-TMD polytype, thus demanding further investigations over TMDs with other arrangements (e.g. 1T or 3R). In particular, 1T-TMDs compounds have attracted interest for understanding the mechanism of charge density wave order at low temperature and its coexistence with superconductivity under high-pressure.[27,28-29] Focusing on the hafnium diselenide (1T-$HfSe_2$), depicted in Figure 1a and 1b, its high carrier mobility (above 2000 $cm^2\ V\ s^{-1}$), significantly larger than that of the 2H-(Mo,W)X_2 (~340 $cm^2\ Vs^{-1}$), is to be highlighted. Due to this extraordinary electronic property, 1T-$HfSe_2$ emerges as one of the most promising material for applications in the ambit of field-effect transistors (FETs).[30,31] Furthermore, the moderate band gap of

1T-$HfSe_2$ (~1.1 eV)[32] opens the possibility of using it as high-κ dielectric leading to the replacement of silicon in electronic devices.[33]

In short, the present study has the aim of providing experimental data and theoretical interpretation on the response of structural, vibrational, and electronic properties of bulk 1T-$HfSe_2$ at hydrostatic high pressures. A homemade diamond anvil cell (DAC) device has been used for performing *in-situ* high pressure measurements, and therefore synchrotron X-ray diffraction, Raman spectroscopy and optical (VIS-NIR) absorption experiments have been carried out. In addition, density functional theory (DFT) based calculations assist and interpret the experiments. Our investigations demonstrate that the 1T-$HfSe_2$ phase is highly sensitive under pressure, reporting a metallization at ~10 GPa, which is actually the lowest value reported to date for bulk TMDs under hydrostatic conditions. Note that this relative low hydrostatic pressure may break down the technological limitations observed in other compounds within the 2H-(Mo,W)$(S, Se)_2$ polytype family, opening new avenues in the generation of novel flexible nanoelectronics devices.

EXPERIMENTAL AND COMPUTATIONAL DETAILS

Samples

$HfSe_2$ samples used in the experiments are acquired from HQGraphene in single crystal form. Pristine single crystal is mechanically exfoliated and cut into smaller pieces in order to obtain various samples of similar dimensions and suitable to be loaded in the high-pressure cells. Crystal structure is checked by room temperature XRD, and purity and homogeneity are probed by Scanning Electron Microscopy (SEM) and X-ray Energy Dispersive Spectroscopy (XEDS). Further details are given in Figure SI1 in the electronic Supplementary Information (SI).

High pressure experiments

Symmetric diamond anvil cells (DAC) are used for high pressure experiments. The general operating scheme of DAC is depicted in Figure 1c. *In situ* high pressure synchrotron X-ray diffraction experiments are performed at beamline ID15B (experiment CH-5079) of the European Synchrotron Radiation Facility. A small piece of $HfSe_2$ is ground into fine powder, subsequently loaded in a membrane-type DAC with 300 μm culet-size diamonds. Stainless steel gasket is pre-indented to 50 μm thick and a hole of 100 μm in diameter is drilled. The sample chamber is filled with helium as pressure transmitting medium (PTM) and two ruby chips for calibrating pressure. The beam operated at 0.411 Å with dimensions close to 5x5 μm^2. Angle-dispersive X-ray patterns are collected with a MAR555 image plate detector. Images are integrated by using both Fit2D and Dioptas software. Rietveld analysis of data is performed through Fullprof software.[34,35]

High pressure Raman experiments are carried out using a Merril-Basset DAC device with 400 μm culet-size. In this case, small single crystal flake of $HfSe_2$ is loaded into the chamber sample of a stainless-steel gasket, as well as Daphne 7373 oil as PTM and ruby chips as pressure markers. XploRA PLUS confocal Raman spectrometer equipped with excitation lines at 532 and 785 nm and several long-distance working objectives is used to acquire the Raman spectra.

Optical absorption under high-pressure conditions is performed on a prototype fiber-optics microscope equipped with two 25× reflecting objectives mounted on two independent *xyz* translation stages for the microfocus beam and the collector objective, and a third independent *xyz* translation stage for DAC micropositioning. Optical absorption data and images are obtained simultaneously with the same device. Spectra in the UV−VIS and NIR are recorded with an Ocean Optics USB 2000 and a

NIRQUEST 512 monochromators using Si- and InGaAs-CCD detectors, respectively. In order to ensure a good quality signal, the absorption spectra are obtained with a $HfSe_2$ single crystal flake with a thickness of around 60 µm. Analysis of data and band gap calculation methodology is detailed in Figure SI2 and Note SI1.

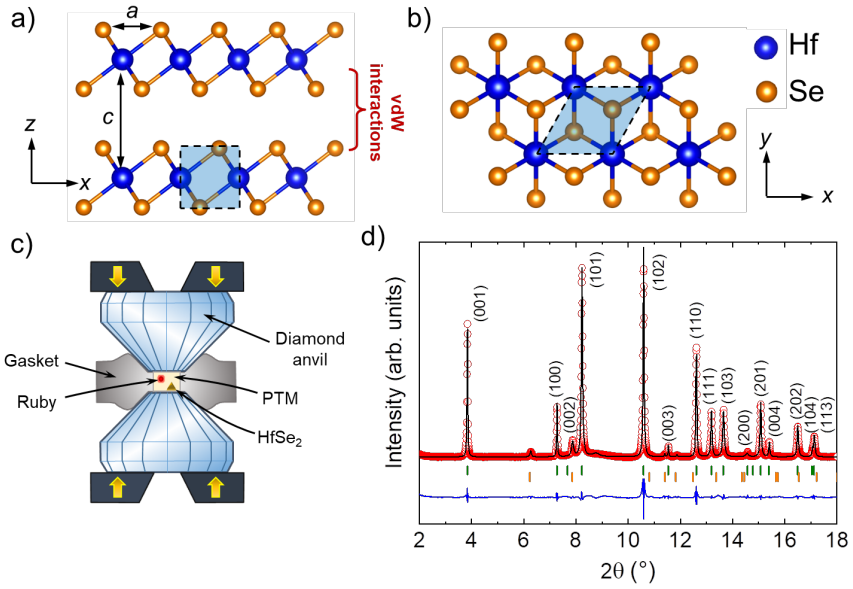

Figure 1. View of the crystal structure of 1T-$HfSe_2$ showing (a) the multilayered arrangement and (b) the *a-b* plane. (c) Schematic of the used high pressure Diamond Anvil Cell set up. (d) Observed (circles), calculated (solid line) and difference (bottom) synchrotron-XRD Rietveld profile for 1T-$HfSe_2$ at room temperature and ambient pressure. Bragg positions indicated in green correspond to 1T-$HfSe_2$, whereas orange marks are due to a very small amount of impurity (less than 3%) identified as metallic Se.

Density functional theory-based calculations

First-principles periodic electronic structure calculations are systematically performed by minimizing static total energies at selected volumes of the 1T-$HfSe_2$ structure. To this end, the Vienna *Ab initio* Simulation Package (VASP)[36] is used employing the Perdew-Burke-Ernzerhof (PBE) implementation[37] within the generalized gradient approximation (GGA) to the exchange-correlation (*xc*) functional. Weak vdW interactions are considered by adding a semi-empirical dispersion potential to the conventional Kohn–Sham DFT energy, through a pair-wise force field following the

Grimme´s DFT-D3 method.[38,39] This dispersion term is highly required to obtain a reasonable agreement with respect to experiments even in dense solids.[40] The Kohn-Sham equations are solved by using an expansion of the valence electron density in a plane-wave basis set with a kinetic energy cut-off of 500 eV. The projector-augmented wave (PAW) method is included to account for the interaction between the valence and the core electron densities.[41,42] Numerical integrations in reciprocal space are carried out by sampling Γ-centered Monkhorst–Pack meshes,[43] where the numbers of subdivisions along each reciprocal lattice vector $\mathbf{b}_i$ were given by $N_i = \max(1.90\ |\mathbf{b}_i| + 0.5)$. The geometry optimizations are considered converged when the forces acting on the nuclei are all below 10^{-5} eV Å^{-1}. Note, however, that this criterion is even tight, 10^{-8} eV Å^{-1}, to calculate the phonon frequencies of Raman active modes at Γ-point by using finite differences as implemented in the VASP package.

In addition, since the standard GGA calculations systematically underestimate the band gap in semiconductor materials, a more sophisticated approach as one based on a hybrid functional would be recommended.[44] A state-of-the-art hybrid-based calculation strategy is followed in this regard to accurately investigate the electronic properties of 1T-$HfSe_2$. Thus, the hybrid HSE06 density functional is selected.[45] By using the hybrid HSE06 functional, 25% of the short-range exchange interaction of the traditional PBE *xc* functional is replaced by the short-range nonlocal Hartree-Fock exchange interaction. In addition, the exchange-screening parameter ω of 0.2 Å^{-1} is applied. Particular numerical integrations by sampling Γ-centered Monkhorst–Pack meshes with $N_i = \max(1.30\ |\mathbf{b}_i| + 0.5)$ are performed.

RESULTS AND DISCUSSION

Structural characterization

To investigate the structure of 1T-$HfSe_2$ and its evolution under hydrostatic pressure conditions, *in situ* high pressure synchrotron X-ray diffraction (XRD) and Raman spectroscopy analysis coupled with DFT-based calculations are carried out. Representative XRD pattern for 1T-$HfSe_2$ at ambient pressure depicted in Figure 1d shows a high crystallinity of the sample. The Rietveld refinement confirms that 1T-$HfSe_2$ belongs to $P\bar{3}m1$ space group containing just one $HfSe_2$ formula unit per the unit cell with trigonal symmetry (see Table S1 for details). The cell parameters are a = 3.7562 Å and c = 6.1749 Å. The internal coordinates are (0,0,0) and (1/3,2/3,0.2560) for Hf and Se, respectively. DFT based calculations predict a = 3.7319 Å, c = 6.2152 Å, and z_{Se} = 0.2538, in good agreement with the experiments. This confirms that the PBE-D3 level of calculation is reasonably reliable to describe the structure of 1T-$HfSe_2$.

As applied pressure increases, the XRD patterns show the well-known shifting towards higher 2θ angles (see Figure SI3). New peaks are not observed during the compression process up to 11.3 GPa and the initial 1T-$HfSe_2$ structure is fully recovered at ambient pressure. Consequently, the compression/decompression cycle is completely reversible (see Figure SI3 and Supplementary Note 2). This outstanding mechanical stability is one of the main desired requirements for the development of future electronic devices operating under harsh conditions.

At this respect, we would like to notice that a pressure-induced phase transition to a C2/m monoclinic structure was recently reported in 1T-$TiTe_2$ showing coexistence with the trigonal phase in a wide range of pressures from ~5 to 19 GPa.[46,47,48] The claimed generality of this transformation in TMD MX_2 compounds was later examined by Mora-Fonz *et al*.[49] The emergence of the monoclinic C2/m structure is explicitly ruled out in their exhaustive computational study of the 1T-$TiSe_2$ polytype. They found that this trigonal structure is the stable phase up to 25 GPa, and conclude that the pressure-

induced polymorphic sequence is still an open question. For 1T-TiS_2, instead of the C2/m monoclinic structure, a cotunnite-like polymorph is proposed as the high-pressure structure where the trigonal polytype transits at 16.2 GPa.[50] The lower oxidation power of Te and the distinctive role of the 5*p* orbital in Te-based TMDs, compared to S and Se counterparts, should be taken into account to explain the rich polymorphism of the TMD family according to the high-pressure study of Léger *et al*. in 1T-$IrTe_2$.[51] Which is of relevance to our work is that in all these experimental and theoretical studies, the trigonal 1T polytype is always observed in the pressure range where experiments and calculations have been performed.

The experimental and computed pressure dependence of the unit cell volume *V*, and lattice parameters *a* and *c* are shown in Figure 2a and 2b, respectively. *V*, *a*, and *c* exhibit smooth variations as pressure increases for both experiments and theory. Computational results are in reasonable agreement with the experiments, although at high pressure the calculated lattice parameter reduction along the interlayer *c*-axis direction is predicted to be slightly higher than the experimental one. This deviation from the experiments can be attributed to the description of the vdW interactions that is reasonable in absence of pressure but is progressively underestimated as pressure increases according to the D3 correction. Overall, the calculated trends observed under pressure are well-described compared to experiments.

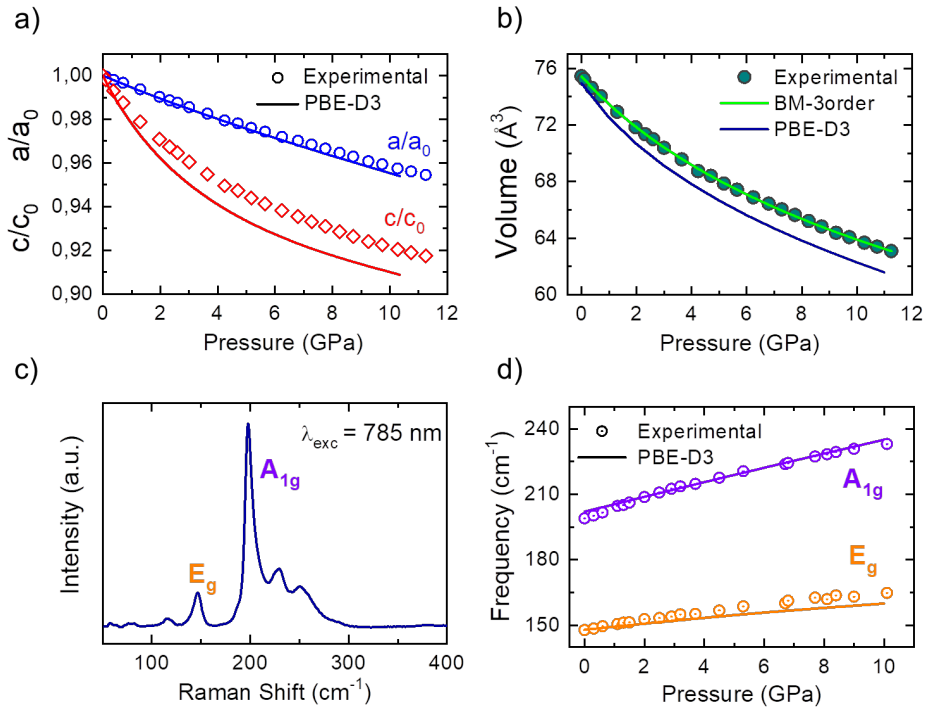

Figure 2. Experimental (from XRD) and theoretical pressure evolution of (a) normalized a/a_0 and c/c_0 lattice parameters and (b) volume of the 1T-$HfSe_2$ unit cell; a third order BM-EOS is also shown in (b). (c) Ambient pressure Raman spectrum of 1T-$HfSe_2$, showing the two main vibrational modes with E_g and A_{1g} symmetry. (d) Evolution of Raman shift frequencies with pressure.

Quantitatively speaking, the pressure evolution of *a*, *c* and *V* is carried out by fitting analytical functions to the data. The experimental third-order Birch-Murnaghan (BM3) equation of state (EOS)[52,53] (see Figure 2b) provides a zero-pressure volume (V_0) equal to 75.42 Å^3, and an isothermal zero pressure bulk modulus (B_0) along with its first pressure derivative (B_0') of 34.5 GPa and 6.9, respectively. DFT calculations lead to V_0= 74.96 Å^3, B_0 = 29.2 GPa and B_0'= 7.0, in reasonable agreement with the experimental results. Here, it must be noted the low B_0 value compared with other compounds within the MX_2 crystal family (for example, 57 GPa and 62 GPa for MoS_2 $MoSe_2$, respectively)[17,19], an interesting result that might anticipate a low metallization pressure for 1T-$HfSe_2$, assuming that the metallization is a consequence of short-distance interlayer interactions.

Concerning the effect of pressure on the unit cell parameters, it is more pronounced in the *c*-axis than in the *a*-axis. The former is reduced around 8.3%, whereas the latter only around half of it, ~4.5%, at the maximum reached pressure in our experiments, close to 11 GPa. Linear isothermal compressibilities (k_i) values of k_a = 5.51 TPa^{-1} and k_c = 21.0 TPa^{-1}, and k_a = 5.51 TPa^{-1} and k_c = 29.6 TPa^{-1} are obtained from the experimental and calculated data, respectively. These values are fully consistent with the trends displayed in Figure 2a, and evidence a clear pressure-induced structural anisotropy in 1T- $HfSe_2$. Likewise, pressure evolution of Se-Se and Hf-Se interatomic distances corroborate this observation, since reduction of Se-Se interlayer distance is much more pronounced than the corresponding to the intralayer Hf-Se one (see Figure SI4). All these structural results have obvious implications in the electronic behavior of this polytype as we will discuss later.

Following with the structural characterization, Raman spectroscopy has been broadly used to characterize TMD-derived materials.[54,55] The Raman spectrum of 1T-$HfSe_2$ (Figure 2c) clearly shows two signals centered at 147 and 199 cm^{-1} corresponding to normal modes of E_g and A_{1g} symmetry in good agreement with previous works.[56,57] The E_g mode corresponds to in-plane vibrations, whereas the A_{1g} one is associated with out-of-plane atomic movements. Interestingly, the DFT-based calculations give frequencies at 148 and 202 cm^{-1}, respectively. Note that the computed Raman frequency modes match quite well in absence of pressure. Not surprisingly, both Raman modes shift towards high frequencies at increasing pressure (Figure 2d). The experimental pressure coefficients for E_g and A_{1g} modes are 1.67 and 3.33 cm^{-1} GPa^{-1}, respectively. Again, our calculations reproduce reasonably well these values. The weak interactions along the *c*-axis direction are significantly sensitive to pressure effects. This structural argument directly explains why the A_{1g} pressure coefficient is higher compared to that of the E_g

mode. The different response of the vibrational modes, depending on whether they are in-plane or out-of-plane, is another manifestation of the pressure-induced anisotropy exhibited by this material (see in Figure SI5 a detailed scheme of normal modes and the Raman spectra under pressure).

Electronic characterization

We show now results from the analysis of the electronic properties of 1T-$HfSe_2$, and more interesting, their evolution under pressure. To this end, *in-situ* high pressure optical absorption experiments coupled with DFT-based electron band calculations are carried out. The VIS-NIR absorption spectra are analyzed in detail (Figure 3a).

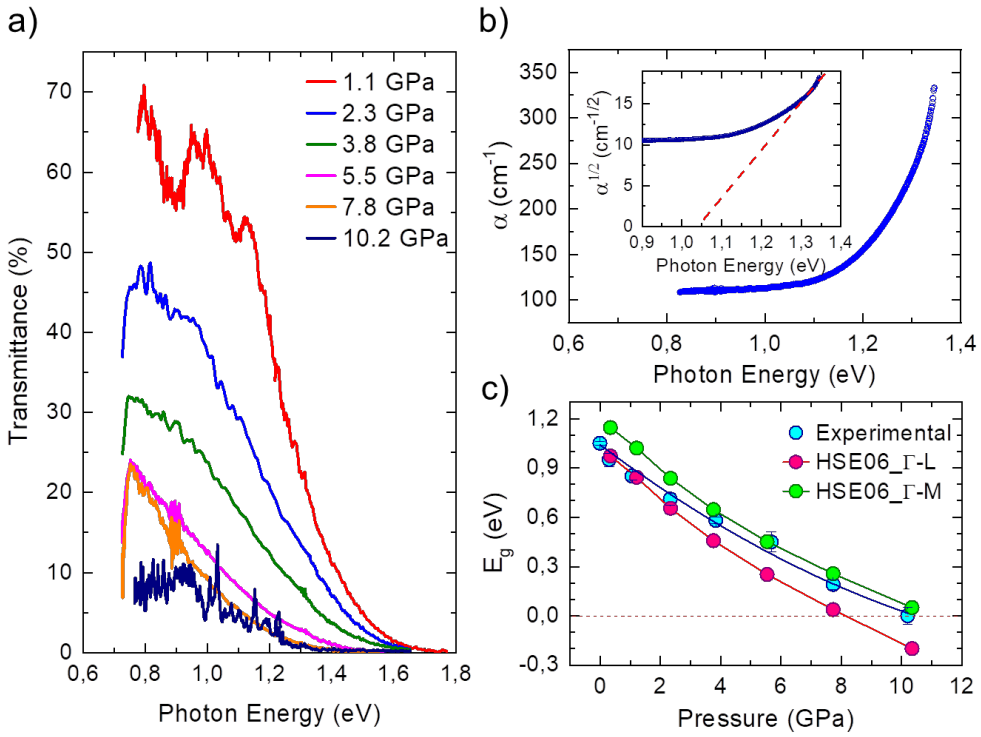

Figure 3. (a) Pressure evolution of the VIS-NIR transmittance spectra for 1T-$HfSe_2$. (b) Optical absorption coefficient *versus* photon energy at ambient pressure (inset shows the linear extrapolation to estimate the band gap). (c) Evolution of the experimental and theoretical calculations of the band gap energy with pressure.

First, we focus on the spectrum in absence of pressure. Plotting the optical absorption coefficient square root *versus* photon energy allows one to estimate the band gap, E_g,

using a linear extrapolation (see details in Figure SI2 and Note SI1). In absence of pressure, 1T-$HfSe_2$ yields to an indirect gap of 1.05 eV estimated by the linear extrapolation (Figure 3b, inset). Our experiments at zero pressure are in good agreement with previous studies.[33,58,59] In addition, accurate DFT-based calculations using the hybrid HSE06 *xc* functional reveal two close indirect gaps at Γ–L (0.97 eV) and Γ–M (1.14 eV) as shown in the band structure depicted in Figure 4a. This leads to a theoretical E_g value of 0.97 eV, in close agreement with the experimental one.

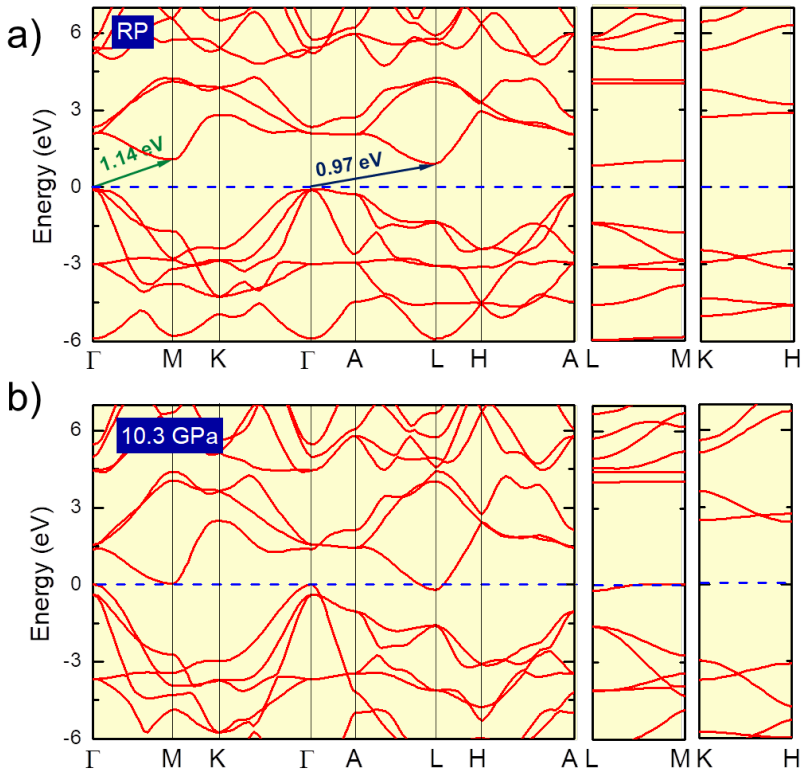

Figure 4. DFT-based calculations of the band structures on 1T-$HfSe_2$ at (a) ambient pressure and (b) metallization pressure. Red line indicates the Fermi level, and arrows show the indirect bandgaps.

The effect of pressure is analyzed based on the VIS-NIR spectra depicted in Figure 3a. A significant reduction of the transmittance within the transmission window below 1.2 eV is observed as pressure increases. Interestingly, the transmission edge becomes almost negligible at 10.2 GPa. This result confirms the closure of the band gap and evidences the metallization of 1T-$HfSe_2$. The linear extrapolation method (see inset in

Figure 3b) has been also used to evaluate the pressure evolution of the band gap. Pressure evolution of the band gap energy is shown in Figure 3c. The E_g narrowing progresses steady and smoothly as the pressure increases. A reduction of 50% in the band gap is already achieved at 4 GPa. The E_g-pressure evolution exhibits an almost linear trend, easily represented with a second order polynomial, similar to other well-known TMDs such as MoS_2 and $MoSe_2$.[17,19]

Further interesting results are found in the analysis of the abovementioned calculated indirect gaps at Γ–L and Γ–M regions of Brillouin zone. The former shows the smallest band gap along the investigated pressure range and disappears at 8.1 GPa, whereas the latter is zero at around 10.9 GPa by an extrapolation analysis (Figure 3c). These computational results pinpoint the emergence of a metal state observed in the experiments and confirm that bulk 1T-$HfSe_2$ becomes metallic at ~10 GPa, the lowest metallization pressure known so far in MX_2 TMDs materials (see Figure 4b).

To identify the atomic orbitals involved in the metallization of 1T-$HfSe_2$, the partial density of states (DOS) depicted in Figure 5 is discussed. This analysis reveals a predominant contribution of the Se 4*p* orbitals in the valence band (VB), whereas the Hf 5*d* orbitals are the ones dominating the conduction band (CB). When 1T-$HfSe_2$ is subjected to high pressure, the contribution from the Se p_z in the VB and that of the metal d_{z^2}, d_{xz} and d_{yz} orbitals in the CB become more important, therefore decreasing the participation of the p_x and p_y orbitals of the chalcogen and the d_{xy} and $d_{x^2-y^2}$ of Hf.

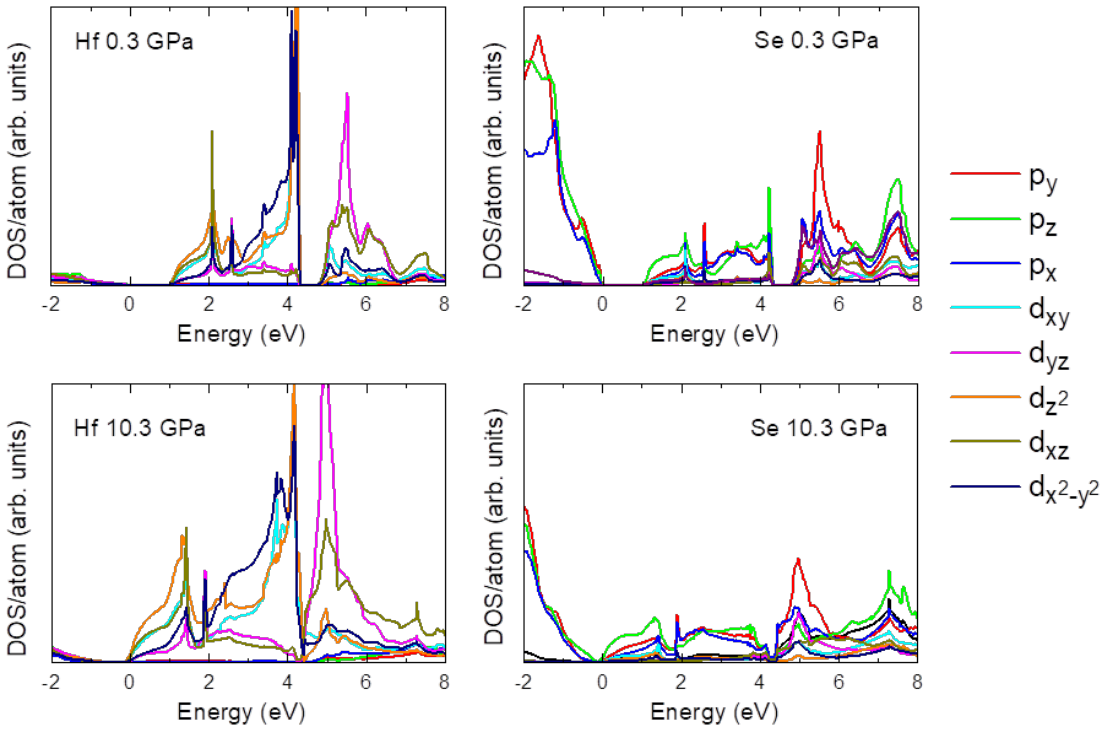

Figure 5. Partial density of states (DOS) for Hf (left) and Se (right) atoms, at 0.3 GPa (upper) and at metallization pressure (lower).

This means that the orbitals with electron density localized along the *z* direction increase their contribution in the density of states of the VB and CB by effect of pressure. This trend is directly connected with the structural anisotropy of this material as described in the previous structural characterization. From the chemical point of view, the hydrostatic pressure induces an effective overlapping between the orbitals directed along *z* direction and, then, non-covalent interactions are strengthened.[26] As a consequence, we conclude that the CB is stabilized thanks to the effective overlapping of theses orbitals, producing the vanishing of the band gap and the eventual metallization of 1T-$HfSe_2$ under pressure.

All these results point out that the metallization of 1T-$HfSe_2$ is conditioned mainly by its response to hydrostatic pressure, and particularly by the compressibility along the *c*-axis. An interesting comparison is schemed in Figure 6a, where the B_0 parameter of different TMDs is included along with our result corresponding to 1T-$HfSe_2$. The latter

presents the lowest B_0 values among the selected TMDs family. It is probably due to a good compromise between the efficient overlapping of the chalcogen's *p* orbitals, which is much more effective in selenides than in sulfides, and the large Hf ionic radius in comparison with other metals as Mo or W. Both factors favor a strengthening of non-covalent interactions along the *z* direction, which justifies a higher compressibility and less rigidity of this material. In fact, such behavior has previously been theoretically predicted by Guzmán *et* al. for TMDs.[60]

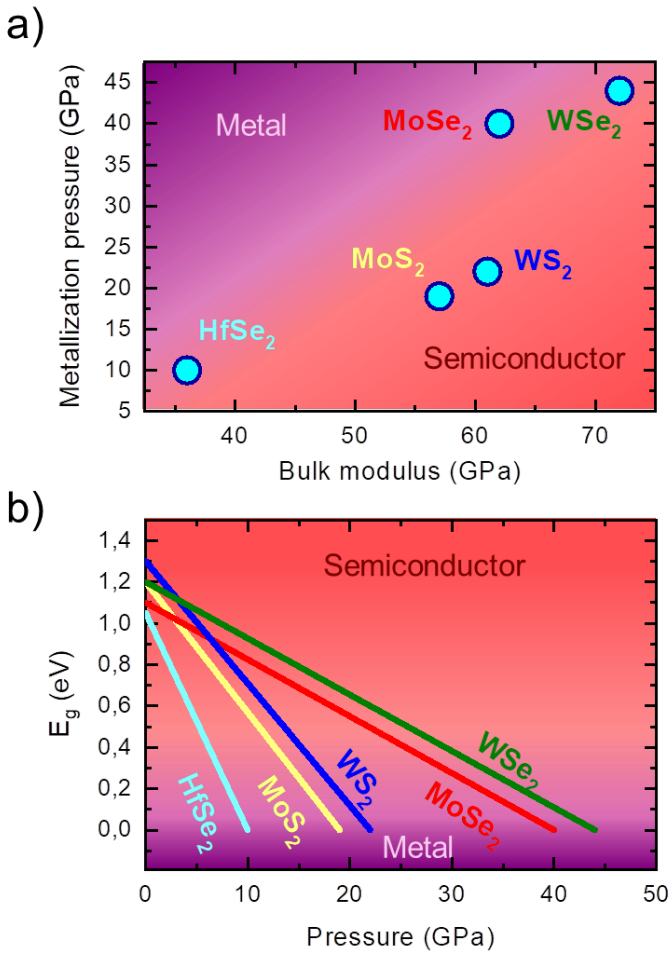

Figure 6. (a) Metallization pressure *versus* Bulk modulus for different TMDs. (b) Evolution of the band gap energy with pressure for different TMDs, showing the metallization pressure for each material.

These results reveal a correlation between the bulk modulus and the metallization pressure for different TMDs explored in Figure 6a. It is clearly seen that the more

compressible is a material, the lower its metallization pressure is expected, and thus 1T-$HfSe_2$ has been positioned in a very attractive pressure regime, close to 10 GPa. 2H-$MoTe_2$, 2H-MoS_2, 2H-MoW_2, 2H-$MoSe_2$, 2H-WSe_2 follow in this order increasing values of both B_0 and P_{met}. Analogously, the bandgap *versus* pressure plotted in Figure 6b show that the linear trends (guide to the eye) of 2H-MX_2 (M=Mo, W; X=S, Se, Te)[17,18,19,20,22,23] and 1T-$HfSe_2$ (this work) also follow the same sequence. Clearly, the reduction of E_g in 1T-$HfSe_2$ occurs at the highest pressure rate, close to 0.1 $eV \cdot GPa^{-1}$. We thus conclude that 1T-$HfSe_2$ presents attractive tunable electronic properties that can be easily modulated by the application of relatively moderate pressures.

CONCLUSIONS

We have undertaken a complete and detailed study on bulk 1T-$HfSe_2$, covering the analysis of its structural, dynamical and electronic properties up to 12 GPa. We have combined experiments and theoretical calculations to shed light on this TMD material in order to understand its behavior under pressure. Our results conclude that 1T-$HfSe_2$ shows a highly sensitive response to pressure application, giving rise to a pressure-driven metallization at around 10 GPa, which is actually the lowest value found to date among common bulk TMDs derived materials. The theoretical calculations are in good agreement with the experimental observations, and the correlation between electronic behavior of the solid and the mechanical response of its crystallographic structure under pressure has been evidenced. Within the studied pressure range there is no first-order structural transition found, and both structure and electronic behavior are completely reversible, which is an essential requirement for the development of future electronic devices operating under harsh conditions. This scenario situates 1T-$HfSe_2$ in a privileged position compared to other TMDs. In fact, most usual strategies for

effectively tuning the electronic properties of these systems concern the dimensionality reduction, working at the nanoscale (monolayers). Through the application of hydrostatic pressure, some materials require even more than 60 GPa for inducing a semiconductor-metal electronic transition. In contrast, 1T-$HfSe_2$ would allow to work within the macroscopic scale, being able to significantly modulate their optoelectronic properties by means of moderate pressure application.

AUTHOR CONTRIBUTIONS

A. A.-C. and J. S.-B. conceived the idea and led the project. A. A.-C. designed the experiments and performed the synchrotron XRD, Raman and optical absorption measurements. A. M.-G., M. A. S., P. P., R. F. and J. M. R. conducted the theoretical calculations. G. G. contributed to the synchrotron XRD measurements at high pressure. J. A. B.-A. and J. G. contributed to the optical absorption experiments at high pressure and analysis of data. M. T. and V. G. B. contributed to the analysis, interpretation and discussion of results. A. A.-C., A. M.-G., J. M. R. and J. S.-B. wrote the manuscript with the help of all the authors. All the authors commented on the final manuscript. J. S.-B. supervised the project.

CONFLICTS OF INTEREST

There are no conflicts of interest to declare.

ACKNOWLEDGEMENTS

We are grateful to Ministerio de Ciencia e Innovación (projects PGC2018-094814-B-C21 and PGC2018-094814-B-C22), Principado de Asturias-FICYT (FC-GRUPIN-IDI/2018/000177) and FEDER (RED2018-102612-T), for the financial support. We are

grateful to ESRF for making all facilities available. A. M.-G. thanks to Spanish MICIUN for a *Juan de la Cierva* postdoctoral contract (IJCI-2017-31979) and *María de Maeztu* MDM-2017-0767 grant.

FIGURE CAPTIONS

Figure 1. View of the crystal structure of 1T-$HfSe_2$ showing (a) the multilayered arrangement and (b) the *a-b* plane. (c) Schematic of the used high pressure Diamond Anvil Cell set up. (d) Observed (circles), calculated (solid line) and difference (bottom) synchrotron-XRD Rietveld profile for 1T-$HfSe_2$ at room temperature and ambient pressure. Bragg positions indicated in green correspond to 1T-$HfSe_2$, whereas orange marks are due to a very small amount of impurity (less than 3%) identified as metallic Se.

Figure 2. Experimental (from XRD) and theoretical pressure evolution of (a) normalized a/a_0 and c/c_0 lattice parameters and (b) volume of the 1T-$HfSe_2$ unit cell; a third order BM-EOS is also shown in (b). (c) Ambient pressure Raman spectrum of 1T-$HfSe_2$, showing the two main vibrational modes with E_g and A_{1g} symmetry. (d) Evolution of Raman shift frequencies with pressure.

Figure 3. (a) Pressure evolution of the VIS-NIR transmittance spectra for 1T-$HfSe_2$. (b) Optical absorption coefficient *versus* photon energy at ambient pressure (inset shows the linear extrapolation to estimate the band gap). (c) Evolution of the experimental and theoretical calculations of the band gap energy with pressure.

Figure 4. DFT-based calculations of the band structures on 1T-$HfSe_2$ at (a) ambient pressure and (b) metallization pressure. Red line indicates the Fermi level, and arrows show the indirect bandgaps.

Figure 5. Partial density of states (DOS) for Hf (left) and Se (right) atoms, at 0.3 GPa (upper) and at metallization pressure (lower).

Figure 6. (a) Metallization pressure *versus* Bulk modulus for different TMDs. (b) Evolution of the band gap energy with pressure for different TMDs, showing the metallization pressure for each material.

REFERENCES

(1) Geim, A. K.; Novoselov, K. S. The Rise of Graphene. *Nat. Mater.* **2007**, *6*, 183-191.

(2) Butler, S. Z.; Hollen, S. M.; Cao, L.; Cui, Y.; Gupta, J. A.; Gutiérrez, H. R.; Heinz, T. F.; Hong, S. S.; Huang, J.; Ismach, A. F.; Johnson-Halperin, E.; Kuno, M.; Plashnitsa, V. V.; Robinson, R. D.; Ruoff, R. S.; Salahuddin, S.; Shan, J.; Shi, L.; Spencer, M. G.; Terrones, M.; Windl, W.; Goldberger, J. E. Progress, Challenges, and Opportunities in Two-Dimensional Materials Beyond Graphene. *ACS Nano*, **2013**, *7*, 2898-2926.

(3) Liu, Y.; Weiss, N. O.; Duan, X.; Cheng, H.-C.; Huang, Y.; Duan, X. Van der Waals Heterostructures and Devices. *Nat. Rev. Mater.* **2016**, *1*, 16042.

(4) Centi, G.; Perathoner, S. Catalysis by Layered Materials: A Review. *Micropor. Mesopor. Mat.* **2008**, *107*, 3-15.

(5) Purdie, D. G.; Pugno, N. M.; Taniguchi, T.; Watanabe, K.; Ferrari, A. C.; Lombardo, A. Cleaning Interfaces in Layered Materials Heterostructures. *Nat. Comm.* **2018**, *9*, 5387.

(6) Choi, W.; Choudhary, N.; Park, G. H.; Park, J.; Akinwande, D.; Lee, Y. H. Recent Development of Two-Dimensional Transition Metal Dichalcogenides and Their Applications. *Mater. Today* **2017**, *20*, 116-130.

(7) Zhang, J.; Peng, Z.; Soni, A.; Zhao, Y.; Xiong, Y.; Peng, B.; Wang, J.; Dresselhaus, M. D.; Xiong, Q. Raman Spectroscopy of Few-Quintuple Layer Topological Insulator Bi_2Se_3 Nanoplatelets. *Nano Lett.* **2011**, *11*, 2407-2414.

(8) Zhou, X.; Cheng, J.; Zhou, Y.; Cao, T.; Hong, H.; Liao, Z.; Wu, S.; Peng, H.; Liu, K.; Yu, D. Strong Second-Harmonic Generation in Atomic Layered GaSe. *J. Am. Chem. Soc.* **2015**, *137*, 7994-7997.

(9) Manzeli, S.; Ovchinnikov, D.; Pasquier, D.; Yazvey, O. V.; Kis, A. 2D Transition Metal Dichalcogenides. *Nat. Rev. Mater.* **2017**, *2*, 17033.

(10) Chhowalla, M.; Shin, H. S.; Eda, G.; Li, L.-J.; Loh, K.-P.; Zhang, H. The Chemistry of Two-Dimensional Layered Transition Metal Dichalcogenides Nanosheets. *Nat. Chem.* **2013**, *5*, 263-275.

(11) Qiu, X.; Ji, W. Illuminating Interlayer Interactions. *Nat. Mater.* **2018**, *17*, 211-213.

(12) Lv, R.; Robinson, J. A.; Schaak, R.; Sun, D.; Sun, Y.; Mallouk, T. E.; Terrones, M. Transition Metal Dichalcogenides and Beyond: Synthesis, Properties, and Applications of Single- and Few-Layer Nanosheets. *Acc. Chem. Res.* **2015**, *48*, 56-64.

(13) Balasubramaniam, B.; Singh, N.; Kar, P.; Tyagi, A.; Prakash, J.; Gupta, R. K. Engineering of Transition Metal Dichalcogenides-Based 2D Nanomaterials Through Doping for Environmental Applications. *Mol. Syst. Des. Eng.* **2019**, *4*, 804-827.

(14) Jung, Y.; Zhou, Y.; Cha, J. J. Intercalation in Two-Dimensional Transition Metal Chalcogenides. *Inorg. Chem. Front.* **2016**, *3*, 452-463.

(15) Liu, F.; Zhou, J.; Zhu, C.; Liu, Z. Electronic Field Effect in Two-Dimensional Transition Metal Dichalcogenides. *Adv. Funct. Mater.* **2017**, *27*, 1602404.

(16) Mao, H.-K.; Chen, B.; Chen, J.; Li, K.; Lin, J.-F.; Yang, W.; Zheng, H. Recent Advances in High-Pressure Science and Technology. *Matter Radiat. Extremes* **2016**, *1*, 59-75.

(17) Nayak, A. P.; Bhattacharyya, S.; Zhu, J.; Liu, J.; Wu, X.; Pandey, T.; Jin, C.; Singh, A. K.; Akinwande, D.; Lin, J.-F. Pressure-Induced Semiconducting to Metallic Transition in Multilayered Molybdenum Disulphide. *Nat. Commun.* **2014**, *5*, 3731.

(18) Nayak, A. P.; Yuan, Z.; Cao, B.; Liu, J.; Wu, J.; Moran, S. T.; Li, T.; Akinwande, D.; Lin, J.-F. Pressure-Modulated Conductivity, Carrier Density, and Mobility of Multilayered Tungsten Disulphide. *ACS Nano*, **2015**, *9*, 9117-9123.

(19) Zhao, Z.; Zhang, H.; Yuan, H.; Wang, S.; Lin, Y.; Zeng, Q.; Xu, G.; Liu, Z.; Solanki, G. K.; Patel, K. D.; Cui, Y.; Hwang, H. Y.; Mao, W. L. Pressure Induced Metallization with Absence of Structural Transition in Layered Molybdenum Diselenide. *Nat. Commun.* **2015**, *6*, 7312.

(20) Liu, B.; Han, Y.; Gao, C.; Ma, Y.; Peng, G.; Wu, B.; Liu, C.; Wang, Y.; Hu, T.; Cui, X.; Ren, W.; Li, Y.; Su, N.; Liu, H.; Zou, G. Pressure Induced Semiconductor-Semimetal Transition in WSe_2. *J. Phys. Chem. C* **2010**, *114*, 14251-14254.

(21) Wang, X.; Chen, X.; Zhou, Y.; Park, C.; An, C.; Zhou, Y.; Zhang, R.; Gu, C.; Yang, W.; Yang, Z. Pressure-Induced Iso-Structural Phase Transition and Metallization in WS_2. *Sci. Rep.* **2017**, *7*, 46694.

(22) Qi, Y.; Naumov, P. G.; Mazhar, N. A.; Rajamathi, C. R.; Schnelle, W.; Barkalov, O.; Hanfland, M.; Wu, S.-C.; Shekhar, C.; Sun, Y.; Süß, V.; Schmidt, M.; Schwarz, U.; Pippel, E.; Werner, P.; Hillebrand, R.; Förster, T.; Kampert, E.; Parkin, S.; Cava, R. J.;

Felser, C.; Yan, B.; Medvedev, S. A. Superconductivity in Weyl Semimetal Candidate $MoTe_2$. *Nat. Commun.* **2016**, *7*, 11038.

(23)Zhao, X.-M.; Liu, H.-L.; Goncharov, A. F.; Zhao, Z.-W.; Struzhkin, V. V.; Mao, H.-K.; Gavriliuk, A. G.; Chen, X.-J. Pressure Effect on the Electronic, Structural, and Vibrational Properties of Layered 2H-$MoTe_2$. *Phys. Rev. B* **2019**, *99*, 024111.

(24) Akinwande, D.; Petrone, N.; Hone, J. Two-Dimensional Flexible Nanoelectronics. *Nat. Commun.* **2014**, *5*, 5678.

(25) Peña-Álvarez, M.; del Corro, E.; Morales-García, Á.; Kavan, L.; Kalbac, M.; Frank, O. Single Layer Molybdenum Disulfide Under Direct Out-of-Plane Compression: Low-Stress Band-Gap Engineering. *Nano Lett.* **2015**, *15*, 3139-3146.

(26) Morales-García, Á.; del Corro, E.; Kalbac, M.; Frank, O. Tuning the Electronic Properties of Monolayer and Bilayer Transition Metal Dichalcogenide Compounds under Direct Out-of-Plane Compression. *Phys. Chem. Chem. Phys.* **2017**, *19*, 13333-13340.

(27) Ritschel, T.; Trinckauf, J.; Garbarino, G.; Hanfland, M.; Zimmermann, M. v.; Berger, H.; Büchner, B.; Geck, J. Pressure Dependence of the Charge Density Wave in 1T-TaS_2 and its Relation to Superconductivity. *Phys. Rev. B* **2013**, *87*, 125135.

(28) Dutta, U.; Malavi, P. S.; Sahoo, S.; Joseph, B.; Karmakar, S. Pressure-Induced Superconductivity in Semimetallic 1T-$TiTe_2$ and Its Persistence Upon Decompression. *Phys. Rev. B* **2018**, *97*, 060503(R).

(29) Sahoo, S.; Dutta, U.; Harnagea, L.; Sood, A. K.; Karmakar, S. Pressure-Induced Suppression of Charge Density Wave and Emergence of Superconductivity in 1T-VSe_2. *Phys. Rev. B* **2020**, *101*, 014514.

(30) Kang, M.; Rathi, S.; Lee, I.; Lim, D.; Wang, J.; Kahn, M. A.; Kim, G.-H. Electrical Characterization of Multilayer $HfSe_2$ Field-Effect Transistors on SiO_2 Substrates. *Appl. Phys. Lett.* **2015**, *10*, 143108.

(31) Yin, L.; Xu, K.; Wen, Y.; Wang, Z.; Huanf, Y.; Wanf, F.; Shifa, T. A.; Cheng, R.; Ma, H.; He, J. Ultrafast and Ultrasensitive Phototransistors Based on Few-Layered $HfSe_2$. *Appl. Phys. Lett.* **2016**, *109*, 213105.

(32) Yue, R. Y.; Barton, A. T.; Zhu, H.; Azcatl, A.; Pena, L. F.; Wang, J.; Peng, X.; Lu, N.; Cheng, X.; Addou, R.; McDonnell, S.; Colombo, L.; Hsu, J. W. P.; Kim, J.; Kim, M.

J.; Wallace, R. M.; Hinkle, C. L. $HfSe_2$ Thin Films: 2D Transition Metal Dichalcogenides Grown by Molecular Beam Epitaxy. *ACS Nano* **2015**, *9*, 474-480.

(33) Mleczko, M. J.; Zhang, C.; Lee, H. R.; Kuo, H.-H.; Magyari-Köpe, B.; Moore, R. G.; Shen, Z.-X.; Fisher, I. R.; Nishi, Y.; Pop, E. $HfSe_2$ and $ZrSe_2$: Two-Dimensional Semiconductors with Native High-κ Oxides. *Sci. Adv.* **2017**, *3*, e1700481.

(34) Prescher, C.; Prakapenka, V. B. DIOPTAS: a Program for Reduction of Two-dimensional X-ray Diffraction Data and Data Exploration. *High Press. Res*. **2015**, *35*, 223–230.

(35) Rodríguez-Carvajal, J. Recent Advances in Magnetic Structure Determination by Neutron Powder Diffraction. *Physica B: Cond. Matter* **1993**, *192*, 55-69.

(36) Kresse, G.; Furthmüller, J. Efficient Iterative Schemes for *ab initio* Total-Energy Calculations Using a Plane-Wave Basis Set. *Phys. Rev. B: Condens. Matter Mater. Phys.* **1996**, *54*, 11169-11186.

(37) Perdew, J. P.; Burke, K.; Ernzerhof, M. Generalized Gradient Approximation Made Simple. *Phys. Rev. Lett.* **1996**, *77*, 3865–3868.

(38) Grimme, S.; Antony, J.; Ehrlich, S.; Krieg, H. A Consistent and Accurate *ab initio* Parametrization of Density Functional Dispersion Correction (DFT-D) for the 94 Elements H-Pu. *J. Chem. Phys.* **2010**, *132*, 154104.

(39) Grimme, S.; Ehrlich, S.; Goerigk, L. Effect of the Damping Function in Dispersion Corrected Density Functional Theory. *J. Comput. Chem.* **2011**, *32*, 1456–1465.

(40) Morales-García, Á.; Illas, F. Comprehensive Analysis of the Influence of Dispersion on Group-14 Rutile-type Solids. *Phys. Rev. Mat.* **2020**, *4*, 073601.

(41) Blöchl, P. E. Projector Augmented-Wave Method. *Phys. Rev. B: Condens. Matter Mater. Phys.* **1994**, *50*, 17953–17979.

(42) Kresse, G.; Joubert, D. From Ultrasoft Pseudopotentials to the Projector Augmented-Wave Method. *Phys. Rev. B: Condens. Matter Mater. Phys.* **1999**, *59*, 1758–1775.

(43) Monkhorst, H. J.; Pack, J. D. Special Points for Brillouin-Zone Integrations. *Phys. Rev. B: Condens. Matter Mater. Phys.* **1976**, *13*, 5188–5192.

(44) Morales-García, Á.; Valero, R.; Illas, F. An Empirical, yet Practical Way To Predict the Band Gap in Solids By Using Density Functional Band Structure Calculations. *J. Phys. Chem. C* **2017**, *121*, 18862-18866.

(45) Krukau, A. V.; Vydrov, O. A.; Izmaylov, A. F.; Scuseria, G. E. Influence of the Exchange Screening Parameter on the Performance of Screened Hybrid Functionals. *J. Chem. Phys.* **2006**, *125*, 224106.

(46) Rajaji, V.; Dutta, U.; Sreeparvathy, P. C.; Sarma, S. Ch., Sorb, Y. A.; Joseph, B.; Sahoo, S.; Peter, S. C.; Kanchana, V.; Narayana, C. Structural, Vibrational, and Electrical Properties of 1T-$TiTe_2$ Under Hydrostatic Pressure: Experiments and Theory. *Phys. Rev. B* **2018**, *97*, 085107.

(47)Zhou, Y.; Chen, C.; Zhou, Y.; Chen, X.; Gu, C.; An, C.; Zhang, B.; Yuan, Y.; Wu, H.; Zhang, R.; Zhang, L.; Zhu, X.; Yang, X.; Yang, Z. Pressure-induced Evolution of Structural and Electronic Properties in $TiTe_2$. *Phys. Rev. B* **2019**, *99*, 125104.

(48) Hu K.; Lian, J.; Zhu, L.; Chen, Q.; Xie, S.-Y. Prediction of Fe_2P-type $TiTe_2$ Under Pressure. *Phys. Rev. B* **2020**, *101*, 134109.

(49) Mora-Fonz, D.; Schon, J. C.; Prehl, J.; Woodley, S. M.; Catlow, C. R. A.; Shluger, A. L.; Sokol, A. A. Real and Virtual Polymorphism of Titanium Selenide with Robust Interatomic Potentials. *J. Mater. Chem. A* **2020**, *8*, 14054.

(50) Yu, F.; Sun, J.-X.; Zhou, Y.-H. The High-pressure Phase Transition of TiS_2 from First-principles Calculations. *Solid State Sciences* **2010**, *12*, 1786.

(51) Léger, J. M.; Pereira, A. S.; Haine, J.; Jobic, S.; Brec, R. Phase Transformations of Polymeric CdI_2-type $IrTe_2$ under high pressure *J. Phys. Chem. Solids* **2000**, *61*, 27.

(52) Birch, F. Finite Elastic Strain of Cubic Crystals. *Phys. Rev.* **1947**, *71*, 809-824.

(53) Murnaghan, F. D. The Compressibility of Media under Extreme Pressures. *Proc. Nat. Acad. Sci.* **1944**, *30*, 244-247.

(54) Zhang, X.; Tan, Q.–H.; Wu, J.-B.; Shi, W.; Tan, P.–H. Review on the Raman Spectroscopy of Different Types of Layered Materials. *Nanoscale* **2016**, *8*, 6435-6450.

(55) Zhang, X.; Qiao, X.-F.; Shi, W.; Wu, J.–B.; Jiang, D.–S.; Tan, P.–H. Phonon and Raman Scattering of Two-Dimensional Transition Metal Dichalcogenides from Monolayer, Multilayer to Bulk Material. *Chem. Soc. Rev.* **2015**, *44*, 2757-2785.

(56) Cingolani, A.; Lugarà, M.; Lèvy, F. Resonance Raman Scattering in $HfSe_2$ and HfS_2. *Physica Scripta* **1988**, *37*, 389-391.

(57) Katkanant, V.; Kirby, R. D. Mixed-Crystal Lattice Dynamics of $Hf_xTi_{1-x}Se_2$. *Phys. Rev. B* **1989**, *40*, 1152-1158.

(58) Greenaway, D. L.; Nitsche, R. Preparation and Optical Properties of Group IV-VI Chalcogenides Having the CdI_2 Structure. *J. Phys. Chem*. **1965**, *26*, 1445-1458.

(59) Gaiser, C.; Zandt, T.; Krapf, A.; Serverin, R.; Janowitz, C.; Manzke, R. Band-Gap Engineering with HfS_xSe_{2-x}. *Phys. Rev. B* **2004**, *69*, 075205.

(60) Guzmán, D. M.; Strachan, A. Role of Strain on Electronic and Mechanical Response of Semiconducting Transition-Metal Dichalcogenide Monolayers: An *ab-initio* Study. *J. Appl. Phys.* **2014**, *115*, 243701.

TABLE OF CONTENTS